OPEN ACCESS
IOP Publishing | International Atomic Energy Agency Nuclear Fusion
Nucl. Fusion **66** (2026) 056033 (12pp) https://doi.org/10.1088/1741-4326/ae5f30

Gyrokinetic simulation of eigenmode GAM in EAST H-mode plasma

Dongxiao Zhang[1,2], Chao Dong[1,2,*], Chu Zhou[3,*], Adi Liu[3], Yifei Ouyang[4], Jian Bao[1,2], Pengfei Liu[1,2], Jintao Cao[1,2], Wenlu Zhang[1,2], Zhihong Lin[5], Ding Li[1,2], Shouxin Wang[6], Hailin Zhao[6] and Haiqing Liu[6]

[1] Beijing National Laboratory for Condensed Matter Physics and Laboratory of Soft Matter Physics, Institute of Physics, Chinese Academy of Sciences, Beijing 100190, China
[2] University of Chinese Academy of Sciences, Beijing 100049, China
[3] School of Nuclear Science and Technology, University of Science and Technology of China, Hefei 230026, Anhui, China
[4] School of Physics, Huazhong University of Science and Technology, Wuhan 430074, China
[5] Department of Physics and Astronomy, University of California, Irvine, CA 92697, United States of America
[6] Institute of Plasma Physics, Chinese Academy of Sciences, Hefei 230021, Anhui, China

E-mail: chaodong@iphy.ac.cn and zhouchu@ustc.edu.cn

Received 5 September 2025, revised 6 March 2026
Accepted for publication 14 April 2026
Published 24 April 2026

Abstract

Gyrokinetic simulations based on the Gyrokinetic Toroidal Code are conducted to investigate the geodesic acoustic mode (GAM) physics in the pedestal of EAST H-mode discharge #74036 (Zhou *et al* 2018 *Nucl. Fusion* **58** 106009). Linear simulations reveal that the instabilities are dominated by the collisionless trapped electron mode (CTEM) in the absence of collisions, and transit to the dissipative trapped electron mode (DTEM) when the collisions are considered. The frequency and propagation direction of DTEM align with those of the edge coherent mode (ECM) observed in the experiments after considering the Doppler shift correction due to the radial electric field on the frequency, indicating DTEM is the dominant component of ECM. In the nonlinear simulations, it is found that CTEM turbulence drives the continuum GAM, whose frequency increases with the ion temperature, aligning with the theoretical predictions. In comparison, DTEM turbulence excites the eigenmode GAM, whose frequency almost does not change with the ion temperature, consistent with the experimental observations. The properties of eigenmode GAM are further confirmed through antenna excitation. Both the continuum and eigenmode GAMs are found to strongly modulate the turbulent transport.

Keywords: H-mode, edge coherent mode, trapped electron mode, eigenmode GAM, shearing rate

(Some figures may appear in colour only in the online journal)

---

[*] Authors to whom any correspondence should be addressed.

1. Introduction

The high-confinement mode (H-mode) [1] is one of the promising operational regimes for future fusion reactors. Characterized by the steep temperature and density gradients in the edge pedestal region, H-mode significantly enhances the core plasma confinement. However, the free energy stored in these steep gradients can drive magnetohydrodynamic (MHD) instabilities, most notably the peeling-ballooning modes [2–4], which are widely recognized as the trigger for edge localized modes (ELMs) [5, 6]. The transient bursts of ELMs can induce large transport and generate unacceptable power loads on the plasma-facing components. Recently, the ELM-free H-mode regimes [7], such as the quiescent H-mode (QH mode) [8], and Enhanced D_α H-mode (EDA H-mode) [9, 10], are becoming more attractive solutions. Accompanying the ELM-free H-mode, the coherent modes are often observed, like the quasi-coherent mode (QCM) in EDA H-mode. These coherent modes, found to be related to trapped electron mode (TEM) [11, 12], can enhance particle transport and maintain edge plasma parameters below the unstable condition of peeling-ballooning mode. Therefore, understanding the excitation of coherent mode and the mechanism of turbulent transport in the pedestal is a critical topic in H-mode physics.

Both the experimental and numerical studies have demonstrated that zonal flow, self-generated by the turbulence, can regulate the saturation level of turbulence through shearing effects [13, 14]. Zonal flow is typically classified into two categories: the low frequency zonal flow (LFZF) and geodesic acoustic mode (GAM) [15, 16] with finite frequencies. Due to plasma inhomogeneity, the GAM frequency generally varies radially, called the continuum GAM. The continuum GAM is particularly prominent in the edge region where the high safety factor (q) decreases the GAM damping rate. The generation mechanism [17, 18] and radial frequency variation [19, 20] of continuum GAM have been extensively studied. The GAM possessing nearly constant frequency with radius, called eigenmode GAM, has also been observed in some devices [21–24] and simulations [25, 26]. Eigenmode GAM can sometimes extend into the core region and is therefore also called global GAM. Despite several theoretical efforts, including those invoking high-order finite Larmor radius (FLR) effects [27, 28] and mode coupling via finite-β effects [29, 30], the generation mechanisms of eigenmode or global GAMs remain inadequately understood. Consequently, further investigation into their excitation and effects on turbulent transport is essential.

In this work, the Gyrokinetic Toroidal Code (GTC) [13, 31] is employed to study the GAM physics in EAST H-mode discharge (shot #74036) [21]. In this discharge, eigenmode GAM is observed for the first time in EAST H-mode operation. It spans the region $\rho \sim 0.95-0.98$ with constant frequency around 21 kHz. The GAM signal is found to be correlated with the edge coherent mode (ECM), whose frequency is about 30–40 kHz, suggesting that eigenmode GAM might be driven by the ECM. In previous researches [32, 33], ECM in EAST is identified as the collisionless trapped electron mode (CTEM) or the dissipative trapped electron mode (DTEM) [34, 35]. CTEM instability arises from the precession resonance of trapped electrons, while DTEM is driven by the dissipative non-adiabatic response of electrons due to the collision detrapping effects. In a recent work, a stationary eigenmode GAM was also discovered near the pedestal top in an EAST H-mode discharge accompanied by a QCM identified as TEM [36]. The connection between TEM and coherent fluctuations is not unique to EAST. The experimental observations in Tore Supra also show that the TEM instability with narrow turbulent spectra is strongly linked to QCM [37, 38]. Motivated by these findings, both from EAST and other devices, we will first examine the linear properties of the instabilities in the pedestal with or without collisions to identify the nature of ECM, and subsequently investigate the GAMs driven by the corresponding turbulence.

The rest of the paper is organized as follows: section 2 introduces the GTC code and simulation parameter settings. In section 3, the linear results of ECM are presented. In section 4, the nonlinear results including the zonal flow shearing rate and electron heat conductivity are shown. Finally, the conclusions are given in section 5.

2. Physical model and parameter settings of the simulation

GTC is a three-dimensional gyrokinetic code for the tokamak physics simulations [13, 31]. The field aligned mesh suitable for general magnetic coordinates enables GTC to efficiently simulate the drift wave instabilities [39, 40], Alfven eigenmodes [41, 42], energetic particle physics [43, 44], and other critical topics in the realistic plasma equilibrium. The capability of GTC to simulate the pedestal instabilities and GAM physics has been verified previously [45–47].

In GTC electrostatic simulations, the gyrokinetic equation is given by [48]:

$$\frac{\mathrm{d}}{\mathrm{d}t} f_\alpha\left(\mathbf{X},\mu,v_\parallel,t\right) \equiv \left[\frac{\partial}{\partial t} + \dot{\mathbf{X}}\cdot\nabla + \dot{v}_\parallel \frac{\partial}{\partial v_\parallel} - C_\alpha\right] f_\alpha = 0, \quad (1)$$

where

$$\dot{\mathbf{X}} = v_\parallel \frac{\mathbf{B_0}}{B_0} + \mathbf{v}_E + \mathbf{v}_d, \quad (2)$$

$$\dot{v}_\parallel = -\frac{1}{m_\alpha}\frac{\mathbf{B}^*}{B_0}\cdot\left(\mu\nabla B_0 + Z_\alpha e\nabla\phi\right). \quad (3)$$

Here α represents the particle species, f_α is the distribution function, $\mathbf{X}$ is the gyrocenter position vector, μ is the magnetic moment, $v_\parallel$ is the parallel velocity, C_α is the collision operator, Z_α is the charge number, m_α is the mass, $\mathbf{v}_E = c\mathbf{b}_0\times\nabla\phi/B_0$ is the $\mathbf{E}\times\mathbf{B}$ drift velocity, $\mathbf{b}_0 = \mathbf{B}_0/B_0$, $\mathbf{B}_0$ is the equilibrium magnetic field, B_0 is its magnitude, ϕ is the perturbed electrostatic potential, $\mathbf{v}_d = (v_\parallel^2\nabla\times\mathbf{b}_0/\Omega_{c\alpha} + \mu\mathbf{b}_0\times\nabla B_0)/(m_\alpha\Omega_{c\alpha})$ is the magnetic drift velocity, and $\Omega_{c\alpha} = Z_\alpha e B_0/m_\alpha c$ is the gyro-frequency.

GTC employs the nonlinear δf method [49] to reduce the numerical noise level. The particle distribution is decomposed into the equilibrium Maxwellian distribution $f_{0\alpha}$ and perturbed part δf_α: $f_\alpha = f_{0\alpha} + \delta f_\alpha$. The time evolution of the perturbed ion distribution δf_i is governed by the gyrokinetic equation. The perturbed electron distribution δf_e is decomposed into the adiabatic part $\delta f_e^{(0)}$ and the kinetic part δg_e. The particle weights for ions and electrons [50] $w_i = \delta f_i / f_i$ and $w_e = \delta g_e / f_e$, respectively, satisfy the following weight equations:

$$\frac{\mathrm{d}w_i}{\mathrm{d}t} = (1 - w_i)\left(-\mathbf{v}_E \cdot \left.\frac{\nabla f_{0i}}{f_{0i}}\right|_{v_\perp} + \frac{Z_i e}{T_i} v_\parallel E_\parallel - \frac{Z_i e}{T_i}\mathbf{v}_d \cdot \nabla\phi\right), \tag{4}$$

$$\begin{aligned}\frac{\mathrm{d}w_e}{\mathrm{d}t} = \quad & \left(1 - \tfrac{\delta f_e^{(0)}}{f_{0e}} - w_e\right)\left(-\mathbf{v}_E \cdot \left.\tfrac{\nabla f_{0e}}{f_{0e}}\right|_{v_\perp} - \tfrac{\partial}{\partial t}\tfrac{\delta f_e^{(0)}}{f_{0e}}\right. \\ & \left. + \tfrac{e}{T_e}\left(\mathbf{v}_d + \mathbf{v}_E\right) \cdot \nabla\langle\phi\rangle\right),\end{aligned} \tag{5}$$

where T_i and T_e are the ion and electron temperatures, respectively, $v_\perp$ is the perpendicular velocity, ϕ is decomposed into the zonal part $\langle\phi\rangle$ and non-zonal part $\delta\phi$ and $E_\parallel = -\mathbf{b}_0 \cdot \nabla\phi$ is the parallel electric field.

The Lorentz collision operator, describing the pitch-angle scattering, is used for the electrons. In the simulations, it is modeled by the following Monte-Carlo operator [51]:

$$\xi_{n+1} = \xi_n\left(1 - \nu_{ei}\Delta t\right) + \left(R_n - 0.5\right)\left[12\left(1 - \xi_n^2\right)\nu_{ei}\Delta t\right]^{\frac{1}{2}}, \tag{6}$$

where ξ_n is the value of the pitch $\xi = v_\parallel / v$ at the nth step, v is the electron velocity, $\nu_{ei} = n_i Z_i^2 e^4 \ln\Lambda / \left(4\pi\varepsilon_0^2 m_e^2 v_{the}^3\right)$ is the electron–ion collision frequency, $v_{the} = \sqrt{2T_e/m_e}$, $\ln\Lambda$ is the Coulomb logarithm, ε_0 is the dielectric constant of the vacuum, Δt is the simulation time step, and R_n is the random number between 0 to 1. For the ions, the collision effects are ignored.

The experiment data of EAST discharge #74036 is used for the simulation. In this discharge, GAM is first observed as continuum GAM in the L-mode stage using the Doppler backscattering (DBS) systems, and temporarily disappears just after L–H transition. In the H-mode stage, GAM reappears and exhibits as eigenmode GAM, which correlates with the ECM. The equilibrium magnetic flux ψ is reconstructed from EFIT based on this discharge at time 1.95 s when eigenmode GAM appears, and the equilibrium density, temperature, and safety factor are shown by the blue curves with circles in figure 1. The uncertainties in n_e and T_e are shown by the error bars. Specifically, the uncertainty in the experimental n_e ranges from 5% to 13% depending on the radial location, and the uncertainty in T_e is approximately 5%. The fitting results of the profiles and the calculated gradients and magnetic shear are represented by the red solid and dashed curves, respectively. In the simulation domain, the fitting profiles lie within the experimental error bars, ensuring consistency with the measured data. The uniform marker particle loading method is employed, in which the density and temperature at the selected equilibrium flux surface are used to represent the whole profile in the weight equations. The radial dependence of density and temperature themselves is not considered as in the previous simulations of pedestal physics using GTC [45], and the accuracy of this approximation has been validated. The radial dependence of plasma profiles is captured by the gradient terms, which are calculated from the real radial profiles of ion and electron. The simulation domain is chosen to be $0.9 < \rho < 0.99$ with ρ being the normalized minor radius, which contains the whole pedestal and the region where eigenmode GAM and ECM are observed. The major radius is $R_0 = 1.88$ m, the minor radius is $a = 0.45$ m, and the on-axis magnetic field is $B_0 = 2.26$ T. T_i is assumed to be equal to T_e. The parameters at the selected equilibrium flux $\rho = 0.98$ are as follows: $n_e = 1.2 * 10^{19}$ m^{-3}, $T_e = 150$ eV, $q = 5.7$, $R_0/L_n = 140$, and $R_0/L_T = 220$. L_n and L_T are the density and temperature scale lengths, respectively. The equilibrium profiles and gradients are fixed in the simulation without considering the relaxation due to turbulent transport. The equilibrium radial electric field E_r is not considered in the simulation. The toroidal mesh consists of 30 grids in each flux surface. The unstructured poloidal mesh consists of 48 radial grids and 2000 poloidal grids at the simulation domain center, with the grid size about $1.0\rho_i$ for the radial direction and $2.0\rho_i$ for the poloidal directions, which is used to simulate the short perpendicular-wavelength modes, where ρ_i is the ion Larmor radius. The time step is $\Delta t = 0.01 R_0/C_s$, with $C_s = \sqrt{T_e/m_i}$ being the sound speed. The particle number per cell is 100 for both ion and electron, and the total particle number per poloidal plane is about 10^6.

3. Linear results

3.1. Linear simulation without collisions

The linear characteristics of ECM without collisions are first investigated. In the case of initial equilibrium profiles, the mode structure is very close to the simulation boundary and significantly influenced by the boundary conditions $\phi = 0$. To eliminate such influence, the magnetic fluxes are extended outward to $\rho = 1.02$ using the spline interpolation and meanwhile the equilibrium density and temperature profiles are shifted inward by $\Delta\rho = 0.02$. The shifted density and temperature profiles and their gradients used in our simulations are indicated by the black solid and dashed curves in figure 1, respectively. The equilibrium flux surface after shifting is at $\rho = 0.96$. In the extended region, the temperature and density gradients are set to zero. This adjusted equilibrium is used in the subsequent simulations.

Simulations incorporating kinetic trapped electrons and adiabatic passing electrons are first conducted. The poloidal mode structure of the electrostatic potential with toroidal mode number $n = 13$ is depicted in figure 2(a). The mode structure spans the region $\rho \sim 0.95 - 0.98$ on the low-field side (LFS). Unlike the conventional ballooning mode structure peaking at the outboard midplane with the poloidal angle $\theta = 0$, this mode peaks at approximately $\theta \approx \pm\pi/4$, which may result from the steep gradients in the pedestal region [33, 45, 52]. The linear growth rate γ and frequency ω versus n are shown as the red curves in figure 3, normalized by C_s/R_0. The mode propagates in the electron diamagnetic drift direction and disappears when the electron kinetic effects are neglected, indicating that

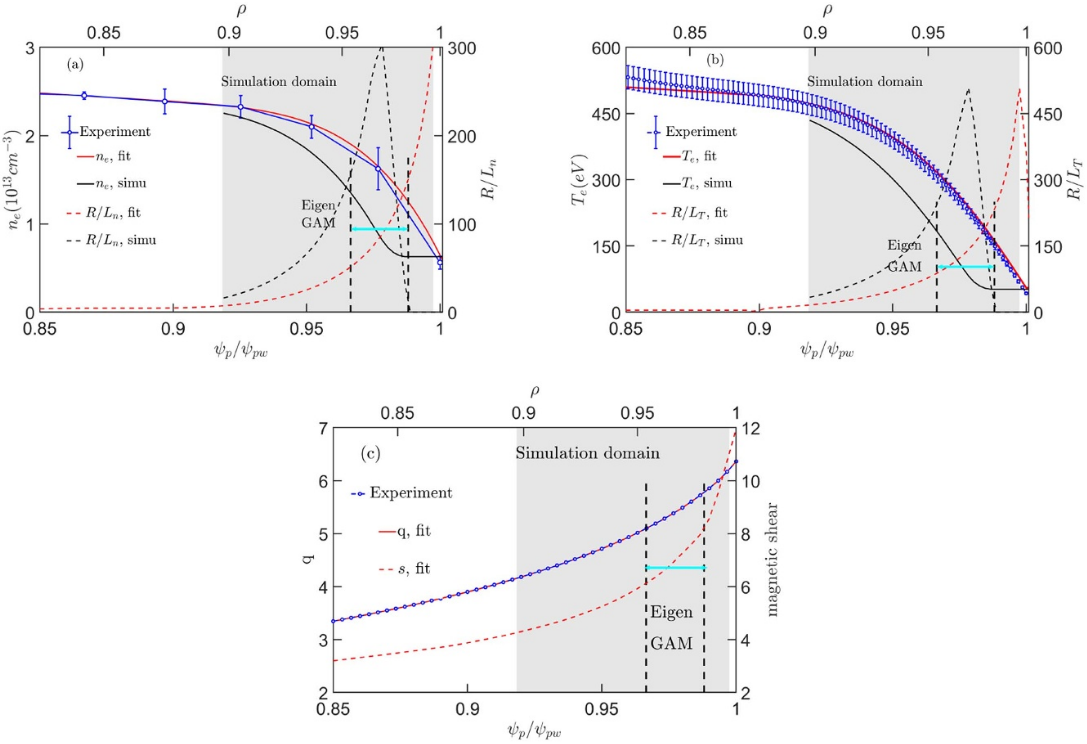

Figure 1. The equilibrium profiles applied in GTC simulations. The blue curves with error bars are the electron density, temperature and safety factor q measured in the experiment. The red solid and dashed curves are the fitting results of the experimental data and the calculated gradients and magnetic shear. The black solid and dashed curves are the inward shifted profiles and their gradients used in the simulation. The shadow areas correspond to the simulation domain. The vertical dashed lines label the area where eigenmode GAM is observed in the experiment.

it is CTEM. Its frequency is of the same order as the electron diamagnetic drift frequency. In comparison, its growth rate is much lower, since the electron precession frequency at the thermal energy is relatively small, allowing only a small fraction of electrons to resonate with the CTEM.

In TEM studies, the response of passing electrons is usually assumed to be adiabatic, as their transit frequency is much larger than the typical CTEM frequency. However, this assumption may not hold in the pedestal. As can be seen in figure 3, the electron transit frequency marked by the star symbol is close to the CTEM frequency. Consequently, the kinetic response of passing electrons should also be considered. Simulations including both kinetic trapped and passing electrons are conducted, and the corresponding mode structure is shown in figure 2(*b*). It can be seen that in addition to the LFS, the mode also appears on the high field side (HFS) due to the kinetic response of passing electrons. The corresponding linear growth rate and frequency in this case are depicted by the blue curves in figure 3. It is shown that the frequency remains almost unaffected, while the growth rate decreases substantially for $n < 60$, indicating that the kinetic passing electrons damp CTEM.

3.2. The collision influence

After examining the CTEM, we investigate the influence of collisions. The typical electron–ion collision frequency is $\nu_{ei} = 5.5C_s/R_0$, corresponding to an effective electron collision frequency $\nu_e^* = \nu_{ei}qR_0/\left(v_{the}\epsilon^{3/2}\right) = 4.1$ with ϵ being the inverse aspect ratio. The poloidal mode structure with collisions for $n = 13$ is shown in figure 2(*c*), which peaks on the HFS. The different mode structure indicates that the instability converts from CTEM to a new mode. To further analyze the collision influence on this mode, we scan ν_{ei} in equation (6) and the scan results are shown in figure 4. As can be seen, for $n = 13$ mode denoted by the red curves, the growth rate increases with ν_{e*} when ν_{e*} is around the experiment range, while the frequency is almost unchanged, indicating that the mode is destabilized by the collisions, consistent with the characteristic of DTEM in previous work [45]. Therefore the mode is identified as DTEM. Furthermore, for $n = 13$ mode, the transition from CTEM to DTEM at a relatively low ν_{e*} (< 1) can also be recognized from the growth rate, which first decreases and then increases with ν_{e*}. Similar phenomena can also be seen for $n = 60$ mode denoted by the blue curves in figure 4 with the transition from CTEM to DTEM occurring at $\nu_{e*} \approx 4$.

From the growth rate and frequency in figure 5, it can be seen that two branches of DTEM coexist at the same radius with similar growth rates for the moderate mode numbers $15 < n < 50$. The frequency of one branch is close to that of CTEM, and the other branch has higher frequency. The mode structure is prevalent on both the HFS and LFS. When $n > 60$, the high frequency branch disappears and collisions begin to damp the mode, leading to lower growth rates. By comparing the cases with and without collisions, the growth rate is higher

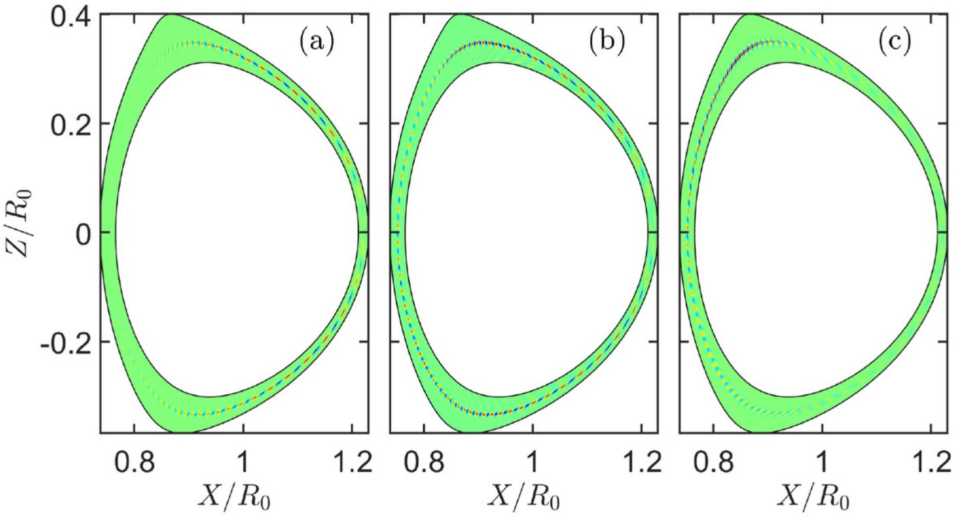

Figure 2. The poloidal mode structure of $n = 13$ perturbed potential for case (*a*) without collisions and with adiabatic passing electrons, case (*b*) without collisions and with kinetic passing electrons, and case (*c*) with collisions.

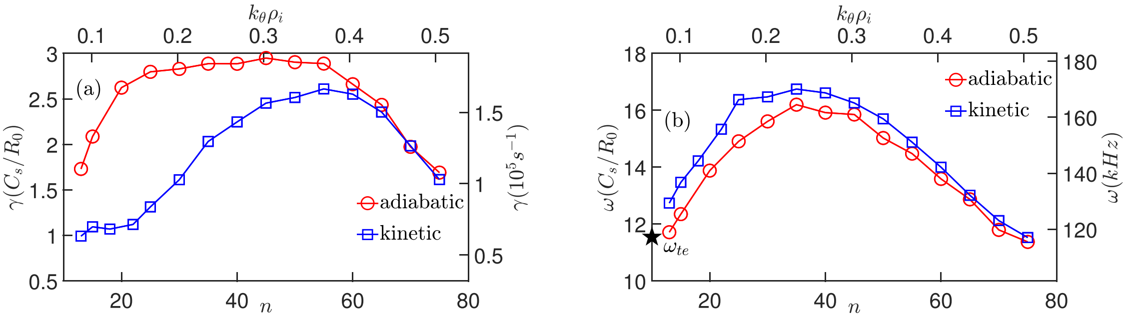

Figure 3. CTEM growth rate (*a*) and frequency (*b*) versus the toroidal mode number *n*. The red curves represent the results with adiabatic passing electrons and the blue curves represent the results with kinetic passing electrons. The black star in (*b*) denotes the electron transit frequency.

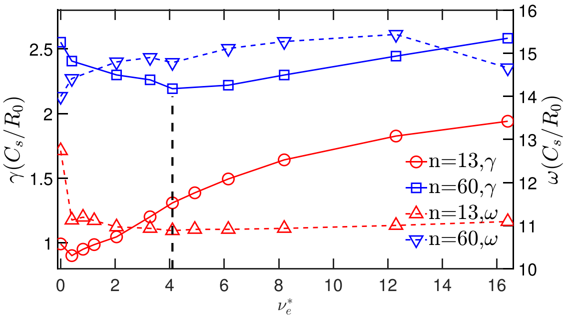

Figure 4. The (solid) growth rates and (dashed) frequencies of (red) $n = 13$ mode and (blue) $n = 60$ mode versus collision frequency. The black vertical line labels the real ν_{e*} in our simulations.

when two branches of DTEM coexist, indicating that DTEM is the main component of the instability in the pedestal. The frequency of simulated DTEM in the range 150–170 kHz is much larger than the ECM frequency 30–40 kHz in the experiment, as the equilibrium radial electric field is not considered in the simulation. After considering the radial electric field induced Doppler shift about 110 kHz, the DTEM and ECM frequencies are comparable. Consequently, the experimentally observed ECM is dominated by DTEM. It is worth pointing out that the shearing rate induced by the equilibrium E_r is about $2.3C_s/R_0$, comparable to the simulation results of the dominant modes with growth rate $\gamma \sim 2.0C_s/R_0$. Moreover, the TEM in our simulations is mainly driven by ∇T_e since $\eta_e = \mathrm{d}\ln T_e/\mathrm{d}\ln n_e > 1$. In this case, the stabilization effects of E_r shear become less important [53]. It is thus believed that the E_r cannot completely suppress TEM.

4. Nonlinear simulation results

4.1. GAM induced by the TEM turbulence

Nonlinear simulations are conducted to investigate the GAM induced by the CTEM and DTEM turbulence. The continuum GAM frequency, scaling as $\sqrt{T_i}$ [19], increases when moving inward from $\rho = 1$, while eigenmode GAM exhibits an almost constant frequency with radius. This feature can generally be used to distinguish them. However, in our simulations, T_i and T_e are taken as constants to avoid the numerical problems arising from their substantial variation over the profiles. Under this condition, the continuum GAM having a constant frequency with radius cannot be distinguished from eigenmode

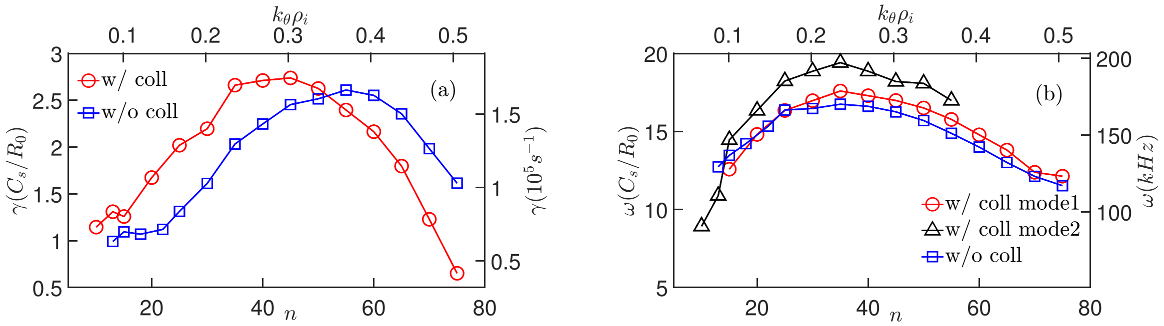

Figure 5. The growth rate (*a*) and frequency (*b*) for DTEM and CTEM with passing electrons versus the toroidal mode number n. The red and black curves in (*b*) represent the coexisting mode frequencies for DTEM.

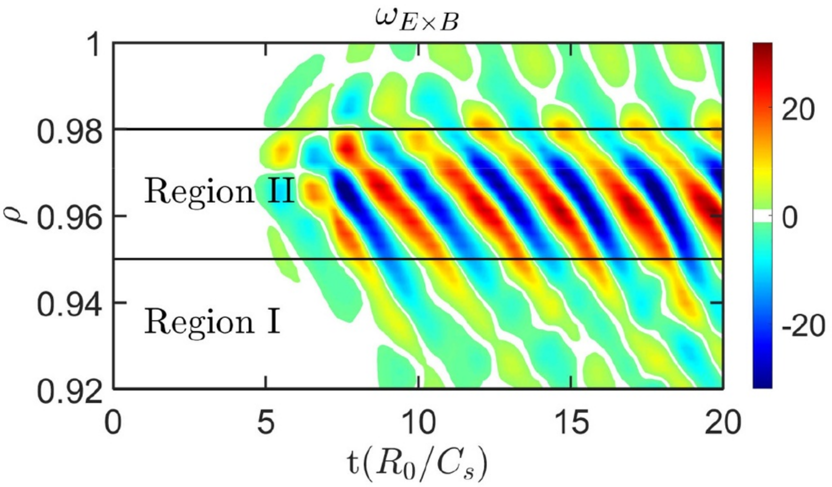

Figure 6. The time-radial structure for zonal flow shearing rate in the CTEM turbulence, and the shearing rate is normalized by C_s/R_0.

GAM. Here, we distinguish them by analyzing their frequency dependence on the ion temperature. The continuum GAM frequency is proportional to $\sqrt{T_i}$ [19, 54, 55]. Varying T_i but fixing its gradient, the GAMs with frequencies aligning with the above scaling law are identified as the continuum GAMs, and those exhibiting weaker dependence on T_i are identified as the eigenmode GAMs.

The nonlinear simulations are first conducted for CTEM with kinetic trapped electrons and adiabatic passing electrons. Both $n = 0$ perturbed density and potential are retained in the simulation. The shearing rate of zonal flow is [56]:

$$\omega_{E\times B} = \frac{(B_\theta R_0)^2}{B_0}\frac{\partial}{\partial\psi}\left(\frac{\partial\langle\phi\rangle}{\partial\psi}\right), \tag{7}$$

which will be used to measure the GAM frequency in the following. The time-radial structure of the shearing rate normalized by C_s/R_0 is shown in figure 6. To better analyze the results, the simulation domain is divided into Region I: $\rho\sim 0.92-0.95$ where the TEM amplitude is relatively small, Region II: $\rho\sim 0.95-0.98$ where the TEM intensity peaks, and the extended region with small gradient, which is excluded from the following discussion. It is found that a regular GAM oscillation emerges in Region II after entering the nonlinear stage, with frequency of about 26 kHz. To explore the dependence of GAM frequency on T_i, we scan the ion temperature. The frequency spectra in Region II for the cases with T_i, $1.4T_i$ and $1.8T_i$ are shown in figure 7, and corresponding GAM frequencies are plotted as the red circles in figure 8. As can be seen, the GAM frequency scales as $\sqrt{T_i}$, consistent with the behavior of continuum GAM [19].

To further identify the GAM nature, the initial perturbation method is used to benchmark the continuum GAM frequency in the realistic experiment equilibrium [54, 55]. In this method, ion guiding centers are initialized with the flux surface averaged density δn_{i00} to generate zonal flow. The density and temperature are set uniform to suppress the turbulence. The time evolution of zonal flow E_r is fitted using the following equation:

$$E_r(t) = A_1 e^{-\gamma_{\mathrm{GAM}} t}\cos(\omega_{\mathrm{GAM}} t + \alpha) + A_2, \tag{8}$$

where ω_{GAM} and γ_{GAM} represent the frequency and damping rate of GAM. The benchmark results of continuum GAM frequency are shown as the black dashed curves in figure 8. The good agreement between the benchmark and simulation GAM frequencies further confirms that CTEM turbulence excites continuum GAM.

For the DTEM turbulence, the zonal flow shearing rate is plotted in the upper panel of figure 9. It is shown that the shearing rate is dominated by LFZF in Region II, while Region I exhibits a weak GAM oscillation. The shearing rate in Region

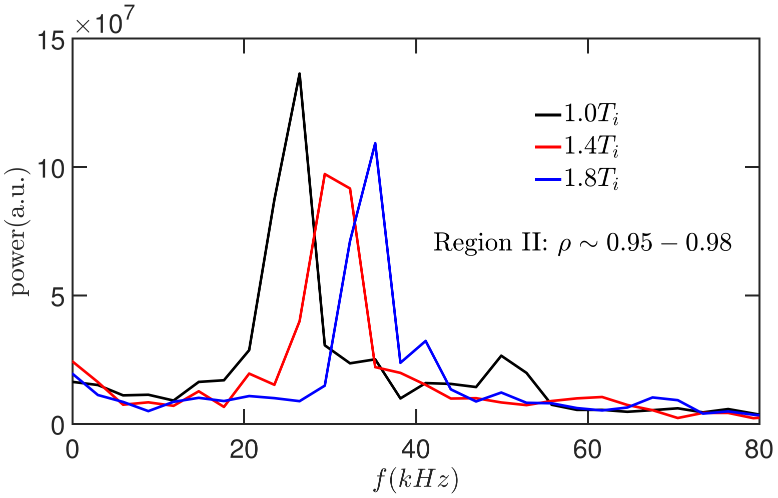

Figure 7. The frequency spectrum of CTEM shearing rate averaged in Region II for cases with $1.0T_i$ (black), $1.4T_i$ (red) and $1.8T_i$ (blue).

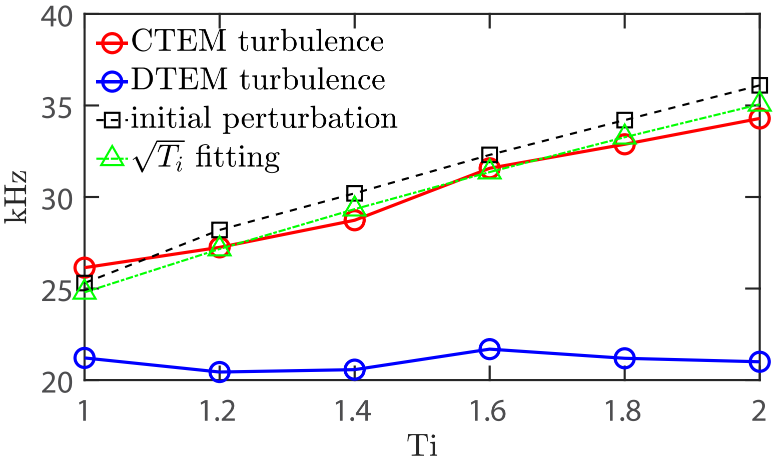

Figure 8. The simulated GAM frequency from CTEM turbulence (red), DTEM turbulence (blue), initial perturbation method (black) and fitting results (green) versus T_i.

I excluding its low frequency component is shown in the lower panel. As can be seen, the GAM oscillation centers around $\rho = 0.94$ and propagates both inward and outward. Figure 10 shows the frequency spectra in Regions I and II for the cases with T_i, $1.4T_i$ and $1.8T_i$. We can see that the GAM frequencies peak around 21 kHz for all cases, matching the eigenmode GAM frequency in the experiment. The scanning results, plotted as the blue curves in figure 8, show that the GAM frequency is insensitive to the ion temperature, indicating that the DTEM turbulence excites eigenmode GAM. The simulated eigenmode GAM location is more inward compared to the experimental results since both the temperature and density profiles in the simulation are shifted inward as shown in figure 1. This shift only changes the location of TEM but scarcely influences its other properties. Additionally, the GAM amplitudes increase for the cases with $1.4T_i$ and $1.8T_i$. In Region II, the case with T_i shows only a 0 kHz peak, representing the LFZF, while for the cases with $1.4T_i$ and $1.8T_i$, eigenmode GAM is also excited. The 0 kHz peak is also observed in the experiment [21]. Besides, a small peak near 45 kHz is observed, which will be investigated in the future. Compared with the shearing rate induced by the CTEM and DTEM turbulence, the equilibrium E_r shear is much smaller, so the neglect of E_r does not influence the turbulence property.

The eigenmode GAM observed in our simulations differs from that reported by Feng *et al* [36]. In their study, the eigenmode GAM at the pedestal top is collisionally damped, whereas in our simulations the eigenmode GAM inside the pedestal is driven by DTEM, indicating that collisions can also excite the GAM. This discrepancy likely arises from two factors: (i) the much lower collision frequency at the pedestal top may not reach the threshold for triggering DTEM, and (ii) the profile gradients differ significantly between the pedestal top and interior, leading to different turbulence regimes.

4.2. Antenna excitation of eigenmode GAM

To validate the eigenmode GAM characteristics, its excitation by the external antenna is conducted. The electrostatic potential of the antenna has a sinusoidal form with frequency ω_{ant}. When ω_{ant} equals the eigen-frequency ω_E of the system, the perturbation amplitude will increase linearly in time

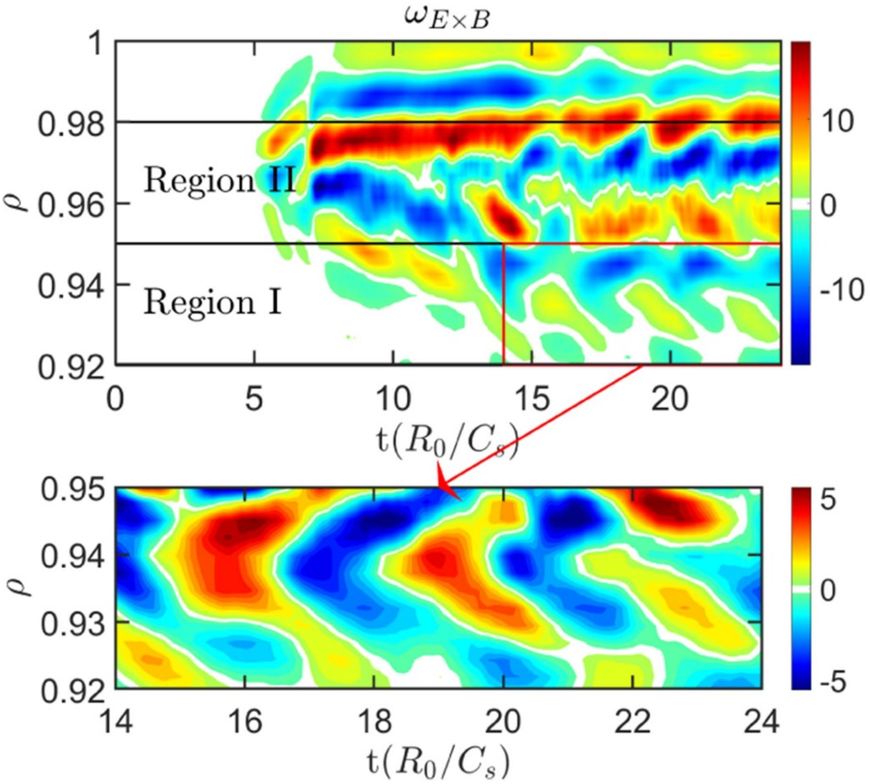

Figure 9. The upper panel denotes the time-radial structure for zonal flow shearing rate in DTEM turbulence. The lower panel denotes the shearing rate in Region I with zero frequency component removed.

with a frequency ω_E until saturation. When ω_{ant} is different from ω_E, the perturbation increases slower in time with frequencies ω_{ant} and ω_E, and saturates at a significantly lower level. In previous studies, the GTC antenna module has successfully excited Alfven eigenmodes and precisely obtained the frequencies [41, 57], and this method has also been used for the research in the kinetic electron response to the external lower hybrid launchers [58, 59].

We conduct simulations with $n/m = 0$ antennas and consider three cases with antenna frequencies 21 kHz, 23 kHz and 26 kHz, respectively. Only the $n = 0$ modes are retained to exclude the turbulence induced GAM. The time evolution and frequency spectra of the antenna driven zonal flow shearing rates are shown in figure 11. It can be seen that when $\omega_{ant} =$ 21 kHz, the shearing rate amplitude first grows linearly with time and finally saturates at a high level, with the dominant frequency matching the eigenmode GAM frequency. When $\omega_{ant} = 23$ kHz or 26 kHz, the shearing rates oscillate with low levels. In the frequency spectra, besides the dominant antenna frequency, a small peak at about 20 kHz exists, close to the eigenmode GAM frequency. These simulation results further confirm the existence of eigenmode GAM in the system.

4.3. Effects of GAM on the turbulence and transport

After identifying the nature of GAMs induced by the CTEM and DTEM turbulence, their modulation effects on the turbulence and transport are studied. The time evolution of the electron heat conductivity χ_e in the CTEM turbulence at $\rho = 0.96$ is shown in figure 12. As can be seen, the turbulence is strongly modulated as the shearing rate of continuum GAM exceeds the linear growth rate. The heat conductivity oscillates at the continuum GAM frequency, and the phase difference between χ_e and GAM remains around $\pi/2$, implying the prey–predator relationship. The local maxima of χ_e roughly corresponds to the zero shearing rate.

For the DTEM turbulence, the large amplitude of LFZF prevents the heat conductivity from oscillating at a specific frequency. To compare the modulation effects of LFZF and eigenmode GAM, simulations without zonal flows are conducted as well. The time-averaged heat conductivities for the cases with T_i, $1.4T_i$ and $1.8T_i$ are shown in figure 13. The solid curves represent the results with zonal flow and the dashed curves the results without zonal flow. The modulation effects manifest as the differences between the solid and dashed curves. In region I where eigenmode GAM dominates for all three cases, zonal flow exhibits similar modulation effects. In region II where zonal flow is dominated by LFZF for the case with T_i as shown previously, the heat conductivities with or without LFZF are at similar levels, implying that the modulation effects of LFZF on the DTEM turbulence and transport are weak. This phenomenon is consistent with the previous studies showing that the effects of LFZF become less important when $\eta_e > 1$ [53]. While for the cases with $1.4T_i$ and $1.8T_i$ where eigenmode GAM appears and has a relatively higher amplitude, the heat conductivities without zonal

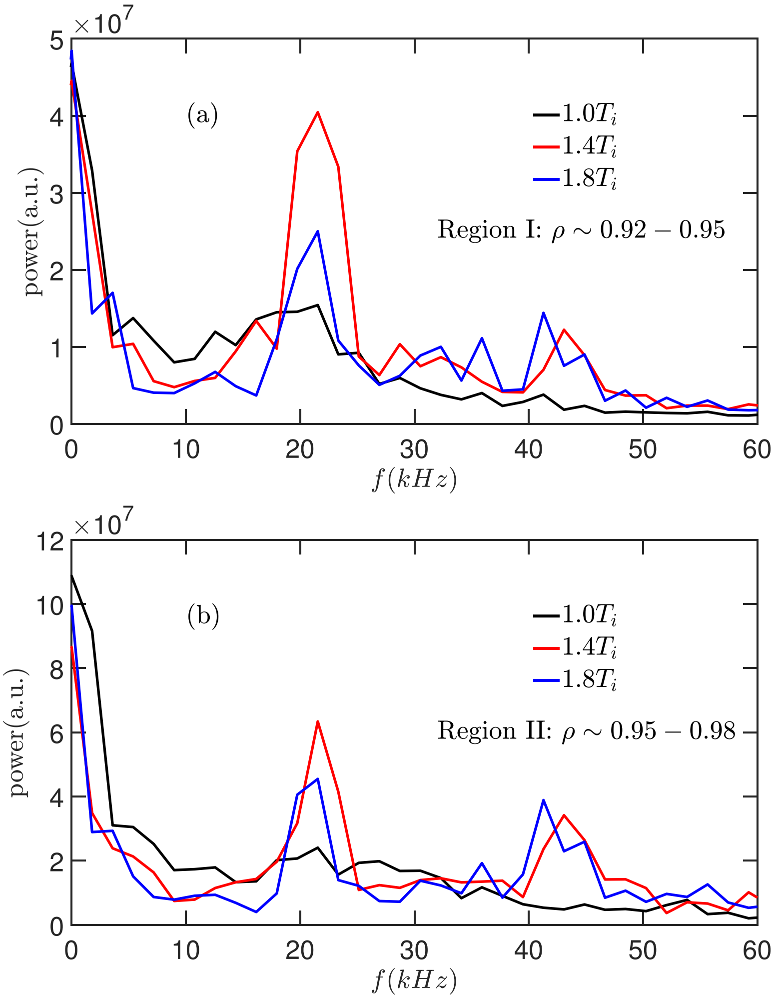

Figure 10. The frequency spectra of DTEM shearing rate averaged in Regions I (*a*) and II (*b*) for cases with $1.0T_i$ (black), $1.4T_i$ (red) and $1.8T_i$ (blue).

flows are larger than those of the T_i case, and drop to a much lower level when zonal flows are included. Considering that the modulation effects of LFZF are weak, the reduction of χ_e indicates that the modulation effects of eigenmode GAM on the DTEM turbulence and transport are significant. By comparing the reduction levels of χ_e between the cases with and without zonal flow, we find that the modulation effects of eigenmode GAM are strengthened when T_i is increased. As ion Larmor radius increases with T_i, the enhancement of eigenmode GAM corresponds to the previous studies that FLR effect is one of the potential driving mechanisms for eigenmode GAM [27, 28].

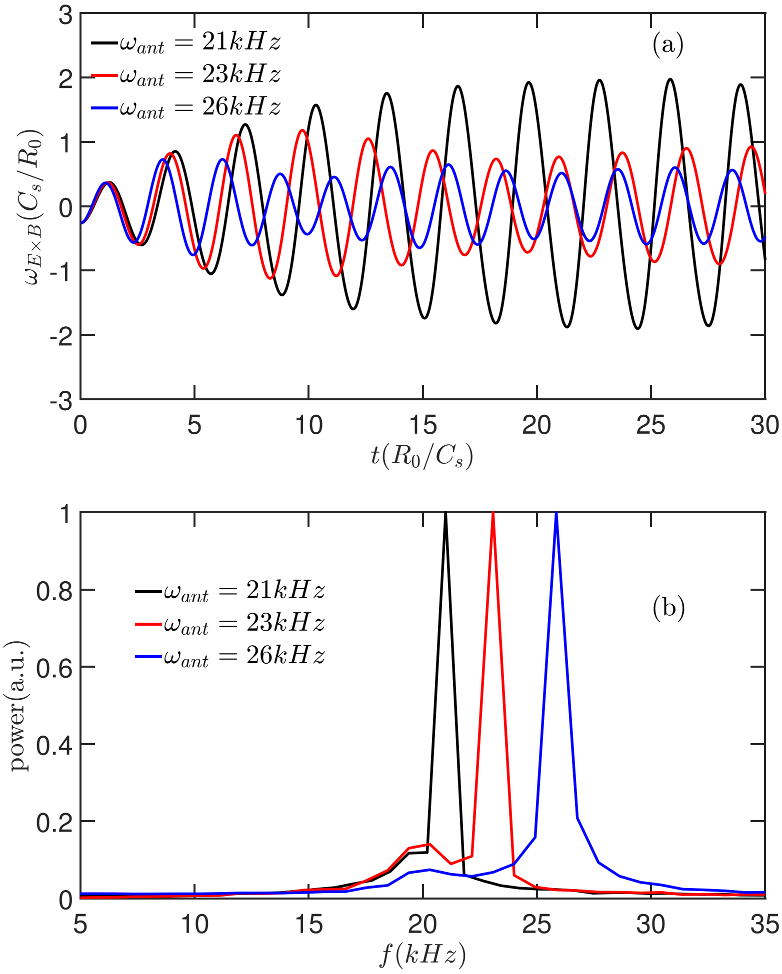

Figure 11. (*a*) The shearing rates excited by the external antennas with $\omega_{ant} = 21$ kHz, 23 kHz and 26 kHz, and (*b*) the corresponding frequency spectra.

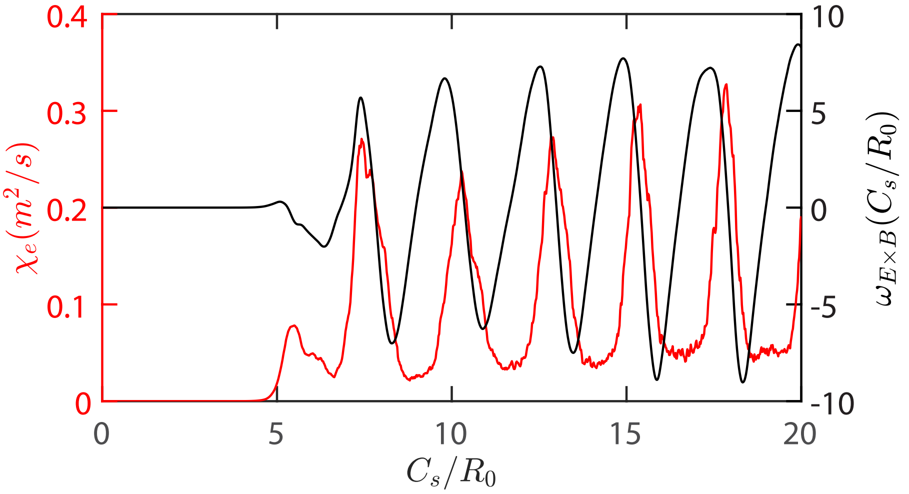

Figure 12. The time evolution of electron heat conductivity (red) and shearing rate (black) at $\rho = 0.96$.

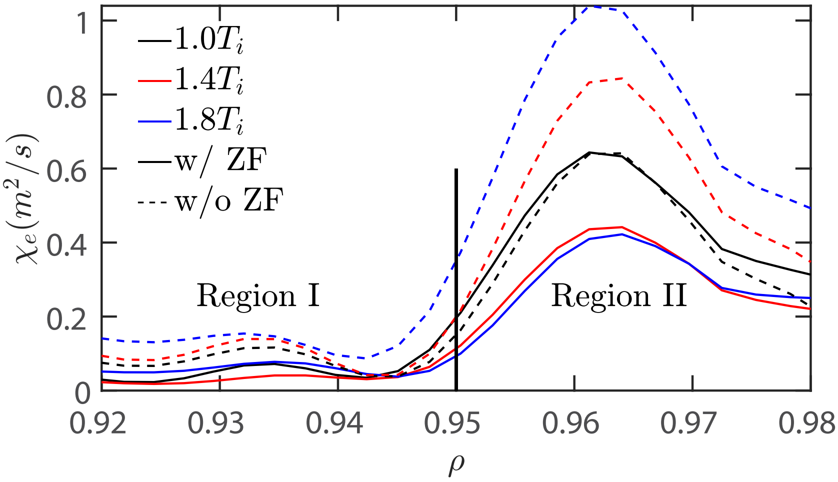

Figure 13. The time-averaged heat conductivities for cases with $1.0T_i$ (black), $1.4T_i$ (red) and $1.8T_i$ (blue). The solid curves represent the results with zonal flows and the dashed curves represent the results without zonal flows.

5. Summary

In this paper, the GAM physics in the EAST H-mode discharge (#74036) are studied using GTC. The linear results show that the collisionless cases exhibit the CTEM instability which is influenced by the kinetic effects of passing electrons, and the collisions trigger the DTEM dominant instability, with two coexisting DTEM branches and growth rate exceeding that of CTEM. From the propagation direction and frequency after Doppler shift correction, we conclude that DTEM is the main component of ECM observed in the experiment. In the nonlinear simulations, it is found that the CTEM turbulence excites continuum GAM. Its frequency dependence on T_i agrees well with the theory, and is validated by the initial perturbation method. Continuum GAM modulates χ_e oscillating at the GAM frequency. The DTEM turbulence is found to excite eigenmode GAM around 21 kHz, which is insensitive to T_i and in good consistency with the experiment results. Eigenmode GAM strongly suppresses the turbulence and transport while the modulation effects of LFZF are weak. These findings indicate that both continuum GAM and eigenmode GAM play important roles in the confinement enhancement of H-mode.

Acknowledgments

This work was supported by the National MCF Energy R&D Program of China under Grant No. 2024YFE03050000, the strategic Priority Research Program of the Chinese Academy of Sciences under Grant No. XDB0500302, and the National Natural Science Foundation of China under Grant Nos. 12025508 and 12475204.

ORCID iDs

Dongxiao Zhang 0009-0009-4931-360X
Chao Dong 0000-0001-8229-2198
Chu Zhou 0000-0003-2928-242X
Adi Liu 0000-0002-3164-7320
Yifei Ouyang 0009-0002-8189-9179
Jian Bao 0000-0002-2890-0700
Pengfei Liu 0000-0002-6739-3684
Wenlu Zhang 0000-0002-7136-2119
Zhihong Lin 0000-0003-2007-8983
Shouxin Wang 0000-0001-9600-4038
Haiqing Liu 0000-0001-6892-358X

References

[1] Wagner F. *et al* 1982 *Phys. Rev. Lett.* **49** 1408
[2] Snyder P., Wilson H., Ferron J., Lao L., Leonard A., Osborne T., Turnbull A., Mossessian D., Murakami M. and Xu X. 2002 *Phys. Plasmas* **9** 2037–43
[3] Snyder P., Wilson H., Ferron J., Lao L., Leonard A., Mossessian D., Murakami M., Osborne T., Turnbull A. and Xu X. 2004 *Nucl. Fusion* **44** 320–8
[4] Snyder P., Wilson H. and Xu X. 2005 *Phys. Plasmas* **12** 056115
[5] Zohm H. 1996 *Plasma Phys. Control. Fusion* **38** 105–28
[6] Leonard A.W. 2014 *Phys. Plasmas* **21** 090501
[7] Paz-Soldan C. (DIII-D Team) 2021 *Plasma Phys. Control. Fusion* **63** 083001
[8] Burrell K., Garofalo A., Solomon W., Fenstermacher M., Orlov D., Osborne T., Park J.-K. and Snyder P. 2013 *Nucl. Fusion* **53** 073038
[9] Greenwald M. *et al* 2000 *Plasma Phys. Control. Fusion* **42** A263–9
[10] Greenwald M. *et al* 1999 *Phys. Plasmas* **6** 1943–9
[11] Macwan T. *et al* 2024 *Phys. Plasmas* **31** 122503
[12] Grenfell G. *et al* 2024 *Nucl. Fusion* **64** 104002
[13] Lin Z., Hahm T.S., Lee W., Tang W.M. and White R.B. 1998 *Science* **281** 1835–7
[14] Diamond P.H., Itoh S., Itoh K. and Hahm T. 2005 *Plasma Phys. Control. Fusion* **47** R35
[15] Winsor N., Johnson J.L. and Dawson J.M. 1968 *Phys. Fluids* **11** 2448–50
[16] Conway G.D., Smolyakov A.I. and Ido T. 2021 *Nucl. Fusion* **62** 013001
[17] Qiu Z., Chen L. and Zonca F. 2014 *Nucl. Fusion* **54** 033010
[18] Zonca F. and Chen L. 2008 *Europhys. Lett.* **83** 35001
[19] Gao Z., Itoh K., Sanuki H. and Dong J. 2008 *Phys. Plasmas* **15** 072511

[20] Gao Z. 2010 *Phys. Plasmas* **17** 092503

[21] Zhou C. *et al* 2018 *Nucl. Fusion* **58** 106009

[22] Wang G. *et al* 2013 *Phys. Plasmas* **20** 092501

[23] Melnikov A. *et al* 2015 *Nucl. Fusion* **55** 063001

[24] Silva C. *et al* 2016 *Nucl. Fusion* **56** 106026

[25] Villard L., Angelino P., Bottino A., Brunner S., Jolliet S., McMillan B.F., Tran T.M. and Vernay T. 2013 *Plasma Phys. Control. Fusion* **55** 074017

[26] Villard L. *et al* 2019 *Plasma Phys. Control. Fusion* **61** 034003

[27] Wang Y., Zhou T. and Wang X. 2021 *Nucl. Fusion* **61** 106024

[28] Wang Y., Zhou T. and Wang X. 2022 *Nucl. Fusion* **62** 106019

[29] Ren H., Wei L., Zhang D. and Xu X. 2020 *Phys. Plasmas* **27** 042504

[30] Ilgisonis V., Khalzov I., Lakhin V., Smolyakov A. and Sorokina E. 2014 *Plasma Phys. Control. Fusion* **56** 035001

[31] Holod I., Zhang W., Xiao Y. and Lin Z. 2009 *Phys. Plasmas* **16** 122307

[32] Wang H. *et al* 2014 *Phys. Rev. Lett.* **112** 185004

[33] Xie B., Ye L., Chen Y., Zhao P., Ye Y., Lin X., Lan H., Guo W. and Xiang N. 2023 *Nucl. Fusion* **63** 026017

[34] Adam J., Tang W. and Rutherford P. 1975 Destabilization of the trapped electron mode by magnetic curvature drift resonances *Technical Report* (Princeton Plasma Physics Laboratory (PPPL))

[35] Connor J., Hastie R. and Helander P. 2006 *Plasma Phys. Control. Fusion* **48** 885

[36] Feng X. *et al* 2025 *Nucl. Fusion* **65** 026036

[37] Arnichand H. *et al* 2015 *Nucl. Fusion* **55** 093021

[38] Arnichand H. *et al* 2016 *Plasma Phys. Control. Fusion* **58** 014037

[39] Xiao Y. and Lin Z. 2009 *Phys. Rev. Lett.* **103** 085004

[40] Ma Y., Zhang B., Bao J., Lin Z., Zhang W., Cai H. and Li D. 2023 *Nucl. Fusion* **63** 056014

[41] Zhang W., Holod I., Lin Z. and Xiao Y. 2012 *Phys. Plasmas* **19** 022507

[42] Liu P., Wei X., Lin Z., Brochard G., Choi G., Heidbrink W., Nicolau J. and McKee G. 2022 *Phys. Rev. Lett.* **128** 185001

[43] Zhang W., Lin Z. and Chen L. 2008 *Phys. Rev. Lett.* **101** 095001

[44] Zhang C., Zhang W., Lin Z. and Li D. 2013 *Phys. Plasmas* **20** 052501

[45] Zhao C., Zhang T. and Xiao Y. 2017 *Phys. Plasmas* **24** 052509

[46] Liu F., Lin Z., Dong J. and Zhao K. 2010 *Phys. Plasmas* **17** 112318

[47] Liao X., Lin Z., Holod I., Li B. and Sun G.Y. 2016 *Phys. Plasmas* **23** 122305

[48] Brizard A.J. and Hahm T.S. 2007 *Rev. Mod. Phys.* **79** 421–68

[49] Parker S. and Lee W. 1993 *Phys. Fluids B* **5** 77–86

[50] Lin Z., Nishimura Y., Xiao Y., Holod I., Zhang W. and Chen L. 2007 *Plasma Phys. Control. Fusion* **49** B163

[51] Lin Z., Tang W. and Lee W. 1995 *Phys. Plasmas* **2** 2975–88

[52] Xie H. and Xiao Y. 2015 *Phys. Plasmas* **22** 090703

[53] Ernst D.R., Lang J., Nevins W.M., Hoffman M., Chen Y., Dorland W. and Parker S. 2009 *Phys. Plasmas* **16** 055906

[54] Zhang H., Qiu Z., Chen L. and Lin Z. 2009 *Nucl. Fusion* **49** 125009

[55] Zhang H. and Lin Z. 2010 *Phys. Plasmas* **17** 072502

[56] Hahm T. and Burrell K. 1995 *Phys. Plasmas* **2** 1648–51

[57] Deng W., Lin Z., Holod I., Wang X., Xiao Y. and Zhang W. 2010 *Phys. Plasmas* **17** 112504

[58] Valade L., Caschera E., Ghendrih P., Sarazin Y. and Ekedahl A. 2016 Electron dynamics in the vicinity of lower hybrid antennas *J. Phys.: Conf. Ser.* **775** 012015

[59] Valade L. *et al* 2018 *Contrib. Plasma Phys.* **58** 465–70